Al - Saeed University Journal of Applied Sciences
journal@alsaeeduni.edu.ye
Vol (9), No(1), Jun., 2026
ISSN: 3104 - 8978 (Print) ISSN: 3104-8986 (Online)

Aurivillius type $BiCrVO_x$ -Catalyzed Photocatalytic degradation of methylene blue in aqueous media under visible- light irradiation

Afraah M. A. Alfaatesh
Department of Chemistry
Faculty of Applied Sciences
Taiz University, Taiz, Yemen

Rokhsana Ismail
Department of Chemistry
Faculty of Education, Aden University, Aden, Yemen

Rawdah Whba
Department of Chemistry
Faculty of Applied Sciences
Taiz University, Taiz, Yemen
Physics Department, Inonu University, Battalgazi
Malatya 44280, Türkiye

Khalid A.S. Alhammadi
Department of Chemistry
Faculty of Applied Sciences
Taiz University, Taiz, Yemen

Niyazi A. S. Al- Areqi
Department of Chemistry
Faculty of Applied Sciences
Taiz University, Taiz, Yemen.
Advanced Research Laboratory
Al- Saeed Center for Scientific Research, Al- Saeed University
Taiz, Yemen
niyazi.alareqi@alsaeeduni.edu.ye

Sameh Alariqi
Department of Chemistry
Faculty of Applied Sciences
Taiz University, Taiz, Yemen
Advanced Research Laboratory
Al- Saeed Center for Scientific Research, Al- Saeed University
Taiz, Yemen

Ahlam Al-Alas
Department of Chemistry
Faculty of Applied Sciences
Taiz University, Taiz, Yemen

Received: 1/3/2026 **Accepted: 5/5/2026**

Journal Website: https://journal.alsaeeduni.edu.ye

Aurivillius type $BiCrVO_x$ -Catalyzed Photocatalytic degradation of methylene blue in aqueous media under visible- light irradiation

Afraah M. A. Alfaatesh
Department of Chemistry
Faculty of Applied Sciences
Taiz University, Taiz, Yemen

Rokhsana Ismail
Department of Chemistry
Faculty of Education, Aden
University, Aden, Yemen

Rawdah Whba
Department of Chemistry
Faculty of Applied Sciences
Taiz University, Taiz, Yemen
Physics Department, Inonu
University, Battalgazi
Malatya 44280, Türkiye

Khalid A.S. Alhammadi
Department of Chemistry
Faculty of Applied Sciences
Taiz University, Taiz, Yemen

Niyazi A. S. Al- Areqi
Department of Chemistry
Faculty of Applied Sciences
Taiz University, Taiz, Yemen
Advanced Research Laboratory
Al- Saeed Center for Scientific
Research, Al- Saeed University
Taiz, Yemen

Sameh Alariqi
Department of Chemistry
Faculty of Applied Sciences
Taiz University, Taiz, Yemen
Advanced Research Laboratory
Al- Saeed Center for Scientific
Research, Al- Saeed University
Taiz, Yemen

Ahlam Al-Alas
Department of Chemistry
Faculty of Applied Sciences
Taiz University, Taiz, Yemen

Abstract

This work reports on a newly developed Aurivillius-type $BiCrVO_x$ series ($Bi_2Cr_xV1\text{-}_xO_{5.5\text{-}x}$, $0.05 \leq x \leq 0.20$), focusing on its phase stability and photocatalytic behavior under visible light irradiation. The samples were synthesized via an ethylene glycol–citrate sol–gel method, followed by microwave-assisted calcination. X-ray diffraction (XRD) and differential thermal analysis (DTA) indicated the stabilization of three crystalline phases, α-monoclinic, β-orthorhombic, and γ-tetragonal, at room temperature. XRD refinement revealed that an increase in chromium content led to lattice expansion owing to the substitution of smaller V^{5+} ions (0.54 Å) with larger Cr^{3+} ions (0.755 Å). The direct band gap energy (Eg), determined by UV–Vis spectroscopy, achieved values ranging from 1.64 to 2.68 eV. The photocatalytic performance was assessed through the

degradation of methylene blue (MB) under visible- light irradiation with $\lambda >$ 400 nm. The highest performance was observed for the γ-tetragonal phase at x = 0.15, with an apparent first-order rate constant (k_{app}) of 13.22 × 10^{-3} min^{-1}. The enhanced activity is attributed to band gap narrowing caused by disordered oxygen vacancies at equatorial sites. In contrast, a decline in performance at x = 0.20 is likely due to vacancy ordering associated with apical oxygen positions. Overall, the results demonstrate that $BiCrVO_x$ is an effective photocatalyst for the removal of recalcitrant organic pollutants from industrial wastewater. 68

Keywords: $BiCrVO_x$, Photocatalytic degradation, MB, XRD, Aurivillius.

Introduction

Synthetic dyes are a key component of industrial effluents, as they are emitted in massive quantities by several manufacturing sectors. The environmental consequences of these dyes are quite concerning due to their potentially carcinogenic properties [1–3]. Recently, various treatment approaches have been developed and employed to eradicate these dyes from wastewater. The methods encompass adsorption, ultrafiltration, reverse osmosis, coagulation, and ion exchange [4–6]. Nevertheless, these techniques do not facilitate the actual destruction of the dye molecules [7,8]. Consequently, considerable emphasis has been placed on identifying alternatives to conventional approaches. One of the promising alternatives is advanced oxidation processes (AOPs), which rely on the chemical, photochemical, or photocatalytic generation of highly reactive species, particularly hydroxyl radicals ($^{\bullet}OH$). These radicals are recognized as strong oxidizing agents capable of degrading a wide range of organic dyes [9]. Consequently, AOPs have been widely reported to achieve high degradation efficiencies and, under optimized conditions, can lead to significant mineralization of pollutants while operating under relatively mild temperature and pressure conditions [10,11]. Numerous metal oxides, including TiO_2, ZnO, ZrO_2, among others, have been extensively studied within AOP frameworks for the photodegradation of synthetic dyes present in wastewater [12,13]. Nevertheless, the high band-gap energy of these materials restricts their activation to ultraviolet light [14], which in turn constrains their commercial use in water and wastewater treatment. To address this limitation, there is a necessity for visible light-induced photocatalysts to enhance the efficiency of AOPs and to effectively degrade these dyes utilizing accessible solar energy.

Our previous studies focused on the electrical properties of oxide–ion conductors, particularly $BiMeVO_x$ materials. In this composition, Bi represents bismuth, Me denotes the dopant metal ion, V refers to vanadium, O_x indicates oxide, and y corresponds to the dopant concentration. These compounds are derived from the partial substitution of Me for V in the parent compound $Bi_2VO_{5.5}$, which possesses a layered Aurivillius-type structure. The results demonstrated that many $Bi_2VO_{5.5}$-based materials exhibit semiconducting behavior at temperatures below 300 °C [15–17].

The first attempt to employ these materials as photocatalysts under visible light was reported by Thakral and Uma [19]. They investigated how $Bi_2VO_{5.5}$ and its modified forms, $BiAlVO_x$ and $BiGaVO_x$, perform under visible-light irradiation, and their study focused on the breakdown of methylene blue (MB) in water-based solutions. These investigations indicated a moderate efficacy for MB photodegradation, demonstrating analogous activities between the Bi_2AlVO_7 and Bi_2GaVO_7 photocatalysts. A subsequent investigation examined the $BiNiVO_x$ analogue for the degradation of a synthetic azo dye [20,21]. This material demonstrated remarkably strong photocatalytic performance. Notably, this high efficiency was achieved even though the compound was prepared using a conventional solid-state synthesis route. Furthermore, a potential mechanism for photocatalytic degradation was proposed and articulated with clarity. Nonetheless, Chen and co-workers [22] explored the photocatalytic activity of hierarchical $Bi_2VO_{5.5}$ hollow microspheres synthesized via a solvothermal route for rhodamine B (RhB) degradation. They found that these microspheres showed higher activity than $Bi_2VO_{5.5}$ powders prepared by conventional methods. Despite several studies reporting the visible-light photocatalytic activity of $Bi_2VO_{5.5}$-based and doped $BiMeVO_x$ systems, these investigations are typically limited to isolated compositions or specific properties, such as band-gap tuning or dye degradation efficiency. However, a systematic and quantitative correlation between phase stability, compositional variation, and photocatalytic performance (e.g., rate constants and band-gap energies) across a defined doping range has not been clearly established [23,24].

Accordingly, this work introduces a new member of the $BiMeVO_x$ family, namely $BiCrVO_x$ ($Bi_2Cr_xV_{1-x}O_{5.5-x}$), which is evaluated for the photocatalytic degradation of MB under visible-light irradiation. In this context, the study systematically investigates the $BiCrVO_x$ system over a controlled compositional range, aiming to elucidate the influence of metal doping on phase stability and photocatalytic properties, while establishing direct correlations between phase evolution, optical characteristics, and photocatalytic performance under identical experimental conditions. Furthermore, particular emphasis is placed on clarifying the relationship between enhanced photocatalytic efficiency and the porosity of the

nanostructured $BiCrVO_x$ phases. The α-monoclinic, β-orthorhombic, and γ-tetragonal phases of $BiCrVO_x$ were obtained through an ethylene glycol-citrate sol-gel synthesis, which was subsequently followed by microwave-assisted calcination. In this study, a range of advanced characterization methods was utilized, including X-ray diffraction (XRD), differential thermal analysis (DTA), Fourier transform infrared (FT-IR) spectroscopy, nitrogen adsorption analysis, and UV-Vis absorption spectroscopy.

Experimental

Preparations of samples

Preparation of $BiCrVO_x$ ($Bi_2Cr_xV_{1-x}O_{5.5-x}$) series; $0.05 \leq x \leq 0.20$

Analytical-grade bismuth(III) nitrate pentahydrate ($Bi(NO_3)_3 \cdot 5H_2O$), ammonium metavanadate (NH_4VO_3), and chromium(III) chloride hexahydrate ($CrCl_3 \cdot 6H_2O$) were used as the precursor chemicals in this work. Individual 0.1 M stock solutions were prepared by dissolving precisely weighed amounts of each compound in deionized water. Citric acid ($C_6H_8O_7$), acting as a chelating agent, was prepared at a concentration of 0.2 M using a deionized water and ethylene glycol mixture in a 3:1 volume ratio. Besides, a 0.5 M ammonia solution (NH_3) was employed to adjust the pH. The precursor solutions were mixed in a volumetric ratio of $2:x:(1-x)$ (Bi:Cr:V) and combined with the citric acid solution to obtain sols. The ratio of citric acid solution to the total concentration of metal ions was fixed at 1.5:1. The pH of the obtained sol systems was precisely regulated to around 7 using NH_3 solution. Subsequently, the sol solutions were heated to 80 °C with continuous stirring for two hours, leading to the formation of a noticeable gel. The wet gels were further subjected to dehydration in an oven at 90 °C for 12 hours to eliminate excess moisture and yield dried xerogels. The xerogel was first finely ground in an agate mortar to ensure homogeneity. It was then calcined using a microwave-assisted method for 55 minutes in a modified oven operating at 2.45 GHz and 100 kW.

Preparation of MB dye solution

A stock solution of MB (0.01 M) was prepared by dissolving exactly 3.1985 g of MB in 1 L of deionized water. Subsequently, a 1.0×10^{-5} M solution was produced by diluting 1.0 mL of this stock to 1 L.

Structural characterization

X-ray powder diffraction (XRD)

XRD patterns were recorded using a Philips PW 1050/30 diffractometer with CuKα radiation (λ= 1.54060 Å). These measurements were used to identify the stabilized phases present and to determine their crystallite sizes and densities. Data were collected in Bragg–Brentano geometry over a 2θ range of 10° to 90°, with a step size of 0.15° and a counting time of 1.3 seconds per step. The unit cell parameters were refined using the X'Pert Plus software.

The average crystallite size(D) was estimated from peak broadening using the Scherrer equation: $D = 0.89\lambda/(B\cos\theta)$, where λ denotes the wavelength of CuKα radiation (λ= 1.54060 Å), B is the the full width at half maximum (in radians), and θ is the diffraction angle.

Thermal analysis

Thermal behavior of the catalyst phases was investigated through differential thermal analysis (DTA) using a Perkin–Elmer instrument. Approximately 20 mg of the dried $BiMeVO_x$ oxide sample was placed in an α-alumina crucible, and measurements were carried out under a flowing nitrogen atmosphere. The gas flow was fixed at 20 ml min^{-1}, while the temperature ranged from ambient temperature to 1000 °Cat at a heating rate of 10 °C min^{-1}. Thermogravimetric analysis (TGA) thermograms of the sample xerogels were obtained under identical conditions.

Fourier Transform – Infrared (FT-IR) Spectrometry

FT–IR spectroscopy was utilized as a methodological approach to elucidate the decomposition processes of xerogels. To prepare transparent pellets, the processed xerogels were mixed with potassium bromide (KBr) at a proportion of 1.5 wt.%. The resulting mixture was then compacted using isostatic pressing under a pressure of 240 Mpa. FT–IR measurements were performed on selected samples after calcination at different temperatures using a Perkin Elmer spectrophotometer. The spectra were recorded in transmittance mode over the wavenumber range of 4000 to 400 cm^{-1}.

Optical Characterization

The optical band-gap energy (E_g) of the sintered photocatalyst samples was assessed from their UV–VIS absorption spectra. Measurements were

carried out at room temperature (RT) using a Shimadzu Scan UV–VIS spectrophotometer (UV-2450 model), covering wavelength interval of 200–800 nm. The direct E_g values were estimated by extending the linear portion of the absorption edge until it intersected the baseline corresponding to zero absorbance (A = 0) [25,26]. The wavelength at the band-edge (λ_g) was employed to compute E_g utilizing the equation:

$$E_g = \frac{1240}{\lambda_g} \qquad (1)$$

Adsorption Measurements

The specific surface areas of the $BiCrVO_x$ photocatalyst samples were determined through nitrogen adsorption–desorption isotherm performed at a temperature of 77 K using an Autosorb-1 instrument (Quantachrome). Adsorption isotherms were recorded over a relative pressure (P/P_o) range of 0.01 to 0.99 under nitrogen. The BET (Brunauer–Emmett–Teller) model was applied to the adsorption data to calculate the specific surface area (SBET), reported, in $m^2\ g^{-1}$.

Kinetics of Photocatalytic Degradation

A 250 mL of MB (1.0×10^{-5} M and pH 10.0) was placed in a 450 mL photoreactor equipped with a magnetic stirring and water refrigeration system. A 100 mg portion of the $BiCrVO_x$ photocatalyst was accurately weighed and added to the dye solution. The resultant suspension was magnetically stirred in the dark environment for 40 minutes to achieve adsorption–desorption equilibrium. A 300-W xenon lamp fitted with an optical glass cut-off filter was used as the visible-light source, providing irradiation with wavelengths above 400 nm. The irradiation source was situated 25 cm above the surface of the liquid in the photoreactor. The temperature of the reaction system was maintained at 25 °C through the circulation of cool water to mitigate any thermal catalytic reaction effects. At 10 min intervals during irradiation, 5 mL aliquots were withdrawn from the photoreactor and filtered to remove catalyst particles.

$$ln\left(\frac{A}{A_o}\right) = -k_{app}t \qquad (2)$$

where A_o and A represent the initial absorbance and the absorbance at irradiation time t, respectively, and k_{app} signifies the apparent first-order rate constant.

Results & discussion

TGA–DTA thermograms of BiCrVO$_x$.10 xerogel

The TGA–DTA profiles of BiCrVO$_x$.10 xerogel (Figure 1) reveal a two-step thermal degradation process occurring between approximately 85 and 420 °C. The first stage degradation is associated with an endothermic peak centered at ~119 °C and corresponds to a weight loss of about 10.7%, which can be attributed to the removal of physically adsorbed water and ammonia species from the xerogel matrix. Partial decomposition of residual ammonium citrate may also contribute to this process [26,27].

The second stage, which occurs between 200 and 420 °C, exhibits a notable exothermic peak at 361 °C along with a notable weight loss (~39.5%). This behavior is likely related to the decomposition and decarbonization of the citrate-based organic matrix, along with possible oxidation of residual nitrogen-containing species [28].

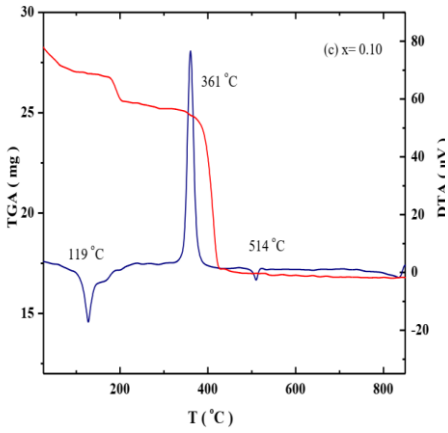

Figure1: TGA – DTA curves of BiCrVO$_x$.10 xerogel.

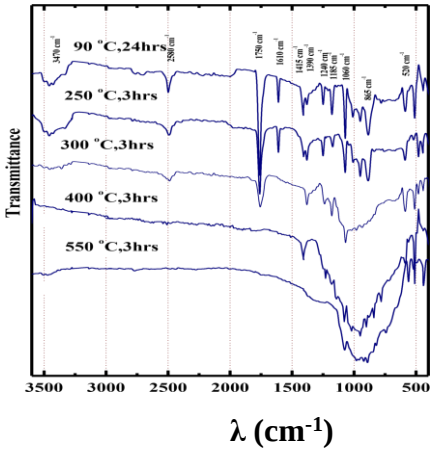

Figure 2: FT–IR spectra of BiCrVO$_x$.15 zerogel calcinated at different temperatures for three hours.

It is imperative to emphasize that the minor endothermic peaks observed in the DTA profiles (Figure 1) at temperatures exceeding 440 °C, without any corresponding mass loss evident in the TGA profiles, are indicative of phase transition phenomena within the BiCrVO$_x$ system.

FT–IR spectra of BiCrVO$_x$.15 xerogel

The thermal degradation of BiCrVO$_x$ xerogels has been further elucidated using FT–IR spectroscopy. For comparison with TGA–DTA

results, Figure 2 presents the FT–IR spectra of **$BiCrVO_x$.15** xerogel calcined at various temperatures for three hours. The dried xerogel exhibits absorption bands corresponding to the precursor metal complexes and residual salts [28]. Specifically, bands at 1415 and 1610 cm^{-1} are attributed to the vibrational modes of the carboxylate groups, although overlapping contributions from nitrate species in the 1390–1415 cm^{-1} region cannot be excluded.

A band located at approximately 1750 cm^{-1} is assigned to C=O stretching vibrations. Vibrational modes associated with metal–oxygen (M–O) bonds, are observed at 1060 and 520 cm^{-1}, corresponding to V-O and Bi-O bonds, respectively. Additional bands at ~1240, 1185, and 1008 cm^{-1} are attributed to C–O stretching, C–H deformation, and O–H bending modes. A broad band centered around 3470 cm^{-1} indicates the presence of adsorbed water and residual NH_3 species. The weak band near 2580 cm^{-1} is more likely related to overtone or combination vibrations rather than fundamental O–H stretching. With increasing calcination temperature up to 250 °C, the main spectral features remain largely unchanged. Howeverat 300 ^oC, most absorption bands shift toward lower wavenumbers and decrease in intensity, reflecting structural changes and progressive decomposition of ammonium citrate and nitrate species. Concurrently, the bands associated with the precursor complex broaden, indicating increased disorder. At 550 ^oC, a broad absorption feature appears in the low-frequency region, characteristic of oxide formation in $BiCrVO_x$, consistent with previous reports for $BiMeVO_x$ systems [29,30]. It is noteworthy that the bands in the frequency regions ~1010 – 820 cm^{-1} and ~640–520 cm^{-1} are assigned to asymmetric stretching and deformation modes of vanadate units in the perovskite–like layers, while bands at ~723 and 431 cm^{-1} are correspond to symmetric V-O and Bi-O, respectively [29].

X-ray Crystallography

The variations in the XRD patterns of the as-synthesized $BiCrVO_x$ photocatalyst series, as a function of Cr substitution, are shown in Figure 3. For the composition with $x = 0.05$, the diffraction pattern can be indexed to the characteristics akin to the distinctive α-phase. This is confirmed by the splitting of the (022)/(220) reflections at $2\theta \approx 32°$, and the (026)/(606) reflections at $2\theta \approx 46.2°$, which are indicative of monoclinic symmetry

(space group Ab2) [31]. For compositions with x = 0.07 and 0.10, the diffraction correspond to the β-phase as evidenced the splitting of the (020)/(200) reflections at 2θ ≈ 32°, along with a single (220) reflection at 2θ ≈ 46.2°, characteristic of orthorhombic symmetry (space group Acam) [6]. It is noted that x = 0.10 lies near the β/γ' phase boundary. For higher compositions (0.10 < $x \leq$ 0.20), the diffraction patterns can be indexed to the γ'-BiCrVOx phase with tetragonal symmetry (space group of I4/mmm), as evidenced by the appearance of a singlet (110) reflection at 2θ = 32° [32].

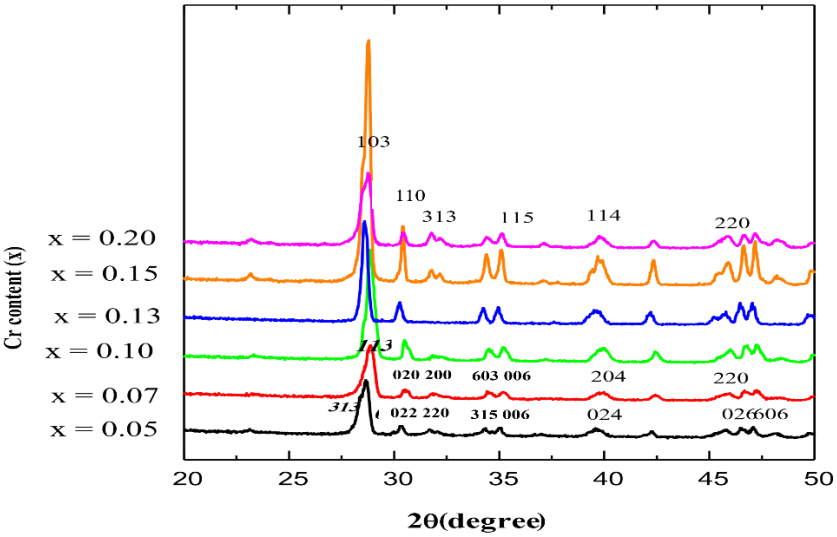

Figure 3: XRD patterns of as– synthesized BiCrVOx photocatalysts.

The The refined unit cell refinement, average crystallite size, and crystallographic density are summarized in Table 1. An increase in lattice parameters, particularly along the a and c axes, is observed with increasing Cr content, resulting in an overall expansion of the unit cell volume. This behavior is attributed to the substitution of V^{5+} ions (≈0.54 Å, CN=6) by larger Cr^{3+} ions (≈0.755 Å), leading to lattice expansion within the perovskite-like vanadate layers [33,34]. A slight decrease in crystallite size (in μm) is observed with increasing Cr concentration. The variation in crystallographic density is primarily governed by changes in lattice parameters and unit cell volume rather than crystallite size.

Table 1.

Refined unit cell parameters, phase stabilizations, average crystallite sizes and crystallographic densities of as– prepared $BiCrVO_x$ series.

x	Unit cell parameters				Phase stabilization		Crystallite parameters	
	a (Å)	b (Å)	c (Å)	V(Å^3)	Phase	Space group	*D* (μm)	d_{XRD} (g cm^{-3})
0.05	5.533	5.628	15.281	475.84	*α*	*Ab2*	3.91	6.87
0.07	5.539	5.613	15.323	476.39	*β*	*Acam*	3.87	6.74
0.10	5.582	5.578	15.591	485.45	*β*	*Acam*	3.88	6.79
0.13	5.616*		15.898	501.41	*γ′*	*I4/mmm*	4.02	6.84
0.15	5.632*		15.887	503.93	*γ′*	*I4/mmm*	3.93	6.78
0.20	5.651*		15.905	507.91	*γ′*	*I4/mmm*	4.17	6.82

*The tetragonal lattice parameter (a_γ) was converted into the mean orthorhombic dimension (a_β) using the relation, $a_\beta = a_\gamma\sqrt{2}$

Differential Thermal Analysis

The thermal stability of the $BiCrVO_x$ system and the enthalpy associated with phase transitions were investigated using DTA thermograms (Figure 4). For the composition with x = 0.05, two distinct endothermic peaks are observed during heating, corresponding to the sequential $\alpha \rightarrow \beta$ and $\beta \rightarrow \gamma$ phase transitions, consistent with typical behavior reported for $BiMeVO_x$ systems. For the composition x = 0.07, a single endothermic peak is observed at 482.73 °C, which is ascribed to the β→γ transition. Similarly, the $BiCrVO_x$ (x = 0.10) sample exhibits a single endothermic peak at 466.3 °C indicating that this composition lies near the β/γ phase boundary. The presence of a single transition peak in these compositions suggests the absence of the α-phase at higher Cr substitution levels.

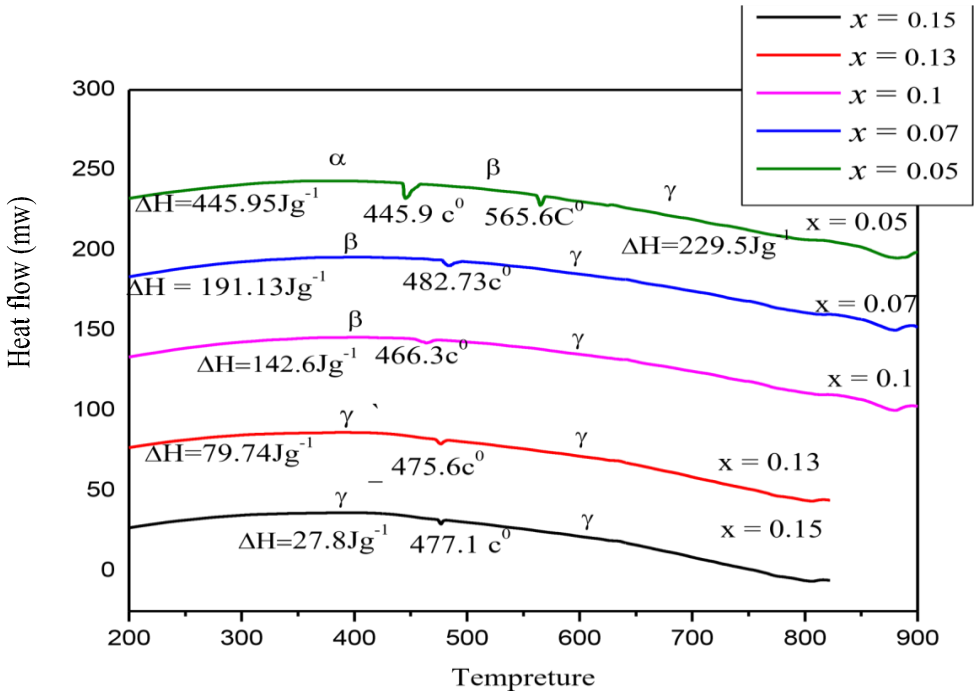

Figure 4: DTA thermograms of as–synthesized BiCrVOx photocatalysts.

The variation of transition temperature (T_t) with increasing Cr content demonstrates an overall increasing trend, which can be attributed to enhanced ordering of oxygen vacancies within the perovskite vanadate layers [35,36]. This phenomenon is consistent with the lattice expansion observed in the XRD results. Furthermore, the transition enthalpy (ΔH_t) decreases with increasing Cr concentration. This reduction in enthalpy change suggests a gradual stabilization of the high-temperature phases. In particular, compositions with $x \geq 0.13$ where the γ' phase is stabilized, exhibit lower ΔH_t values, indicating reduced structural changes during phase transitions and improved thermal stability of the γ'-BiCrVO$_x$ phase [37,38].

Surface and Optical Characteristics of BiCrVO$_x$ Photocatalysts

Figure 5 illustrates the UV-VIS absorption spectra of the BiCrVO$_x$ across different compositions. The absorption edges of the doped samples are shifted relative to that of undoped $Bi_2VO_{5.5}$, indicating that Cr substitution influences the optical properties and enhances visible-light absorption [39]. Among the studied compositions, the samples with x = 0.13 and x = 0.15 exhibit relatively higher absorbance values.

The estimated E_g, along with their corresponding correlation coefficients (R^2), are summarized in Table 2. The band-gap energy initially increases with ascending Cr content up to x = 0.10, followed by a decrease to approximately 1.851 eV (x = 0.13) and 1.64 eV (x = 0.15) before increasing again to 2.68 eV for x = 0.20. The reduction in the E_g at intermediate compositions is likely associated with the stabilization of the γ′ phase and the presence of defect states, such as oxygen vacancies, which introduce localized energy levels within the band gap. At higher Cr concentrations (x = 0.20), the increase in E_g may be attributed to increased structural ordering or reduced defect density. A semi-quantitative estimation of relative crystallinity was performed using the ratio of peak intensities:

$$Crystallinity\ (\%) = \frac{I(0.15)}{I(0.20)} \times 100 \qquad (3)$$

where I(0.15) and I(0.20) correspond to the intensities of (103) reflection for γ′-BiCrVO$_x$ (x = 0.15) and (x = 0.20), respectively. Significantly higher intensities of the (103) and (110) reflections, characteristic of the γ′-tetragonal phase, are observed for the x = 0.15 sample compared to x = 0.20, indicating improved crystallinity and structural ordering.

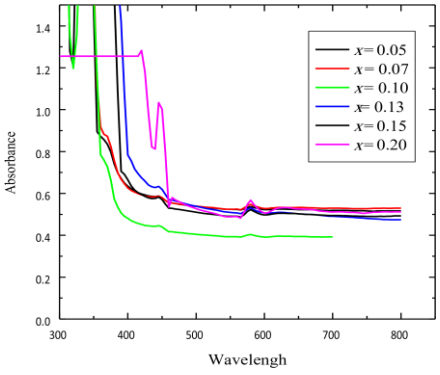

Figure 5: UV–VIS absorption spectra of the BiCrVO$_x$ photocatalysts.

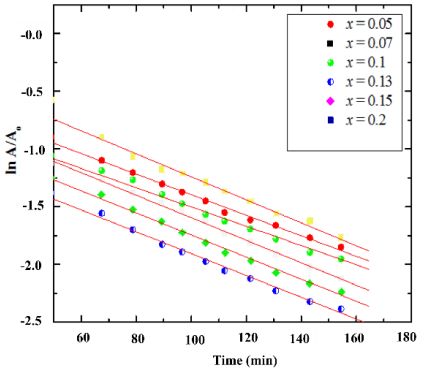

Figure 6: Photocatalytic activities of the BiCrVO$_x$ catalyst series for the degradation of MB dye solution under visible light irradiation.

The BET surface areas (S_{BET}) values listed in Table 2 are relatively similar across all compositions, suggesting that surface area is not the dominant factor governing photocatalytic performance. Instead, the

enhanced activity is more likely associated with modifications in electronic structure and defect chemistry induced by Cr substitution.

Furthermore, adsorption of MB dye onto the catalyst surface is facilitated by the electrostatic interactions between positively charged dye molecules and negatively charged oxygen sites or vacancies in the $BiCrVO_x$ structure. The layered Aurivillius-type structure provides accessible active sites, contributing to improved photocatalytic performance.

Photocatalytic Efficiency of $BiCrVO_x$ Photocatalyst Series

The photocatalytic activity of the synthesized $BiCrVO_x$ compositions was systematically evaluated through the degradation of MB under visible-light irradiation using equal catalyst loadings. The degradation kinetics follow a pseudo-first-order kinetics, as illustrated in Figure 6, where the linear fits indicate good agreement with experimental data. The corresponding apparent rate constants (k_{app}) and R^2 are summarized in Table 2.

The variation in photocatalytic activity across compositions reveals two regions of relatively lower performance, observed at $x = 0.10$ (β-phase) and $x = 0.20$ (γ'-phase). For the β-$BiCrVO_x$ ($x = 0.10$) sample, the lowest degradation rate ($k_{app} = 6.91 \times 10^{-3}$ min^{-1}) is obtained despite its relatively high surface area. This reduced activity is primarily associated with its larger band gap (~2.65 eV), which limits visible-light absorption and charge carrier generation. Similarly, the γ'- $BiCrVO_x$ ($x = 0.20$) sample exhibits a low degradation rate ($k_{app} = 6.82 \times 10^{-3}$ min^{-1}), which can be attributed to its relatively large band gap (~2.68 eV) and possible changes in defect structure. In contrast, enhanced photocatalytic performance is observed within the γ'-phase region, particularly for $BiCrVO_x$ ($x = 0.15$), which exhibits the highest k_{app} value. This improvement is associated with its lower band gap and the presence of a higher concentration of oxygen vacancies. These vacancies introduce localized energy levels within the band structure, which promote charge separation and suppress electron–hole recombination, thereby enhancing photocatalytic activity [39].

Table 2.

Estimated special surface area, band–gap energies and photodegradation rate constants of MB dye by $BiCrVO_x$ series under visible light irradiation.

x	S_{BET} ($m^2\ g^{-1}$)	R^2	E_g (eV)	R^2	$k_{app} \times 10^{-3}$ (min^{-1})	R^2
0.05	0.39	0.9994	2.21	0.9036	7.88	0.9984
0.07	0.31	0.9990	2.52	0.9505	8.94	0.9862
0.10	0.36	0.9986	2.65	0.9110	6.91	0.9874
0.13	0.28	0.9992	1.851	0.9362	8.96	0.9895
0.15	0.26	0.9993	1.64	0.9076	13.22	0.9108
0.20	0.23	0.9988	2.68	0.9837	6.82	0.9877

The distribution of oxygen vacancies also plays a critical role in determining photocatalytic performance. At intermediate Cr concentrations, vacancies are likely more uniformly distributed within the equatorial planes of the perovskite-like layers, facilitating adsorption and catalytic reactions. At higher Cr content, increased vacancy ordering may reduce the number of accessible active sites, thereby limiting photocatalytic efficiency [27]. The photocatalytic degradation mechanism involves both intrinsic semiconductor excitation and dye-sensitized pathways. Under visible-light irradiation, electrons are excited from the valence band (VB) to the conduction band (CB) of $BiCrVO_x$, generating electron– hole pairs. Simultaneously, MB molecules may absorb visible light and transfer excited electrons to the CB of the catalyst. The photogenerated electrons react with dissolved oxygen to form superoxide radicals ($\bullet O_2^-$), while the holes oxidize water or hydroxide ions to generate hydroxyl radicals (•OH). These reactive oxygen species are responsible for the degradation and mineralization of MB dye [40, 41]. Overall, the photocatalytic performance of the $BiCrVO_x$ system is governed by a combination of band gap energy, defect chemistry, and vacancy distribution rather than surface area alone. Among the studied compositions, γ'-$BiCrVO_x$ (x = 0.15) exhibits the most favorable balance of these factors, resulting in superior visible-light photocatalytic activity.

Conclusion

In this study, Aurivillius-type $BiCrVO_x$ ($Bi_2Cr_xV_{1-x}O_{5.5-x}$) photocatalysts were successfully synthesized via an ethylene glycol–citrate sol–gel method followed by microwave-assisted calcination. This approach enabled good phase purity-controlled composition over the range $0.05 \leq x \leq 0.20$.

Structural analysis using XRD and DTA demonstrated that Cr substitution stabilizes the α-monoclinic and β-orthorhombic phases at low dopant levels, while promoting the formation of the γ'-tetragonal phase at higher concentrations.

Optical studies revealed a non-linear dependence of E_g, on Cr content, with noticeable band gap narrowing for compositions in the γ' phase region (x = 0.13 and 0.15). This behavior is attributed to structural phase evolution and the presence of defect states, particularly oxygen vacancies, which modify the electronic structure and enhance visible-light absorption. The photocatalytic activity toward MB was found to depend strongly on phase composition. Among the studied samples, γ'- $BiCrVO_x$ (x = 0.15) exhibited the highest activity ($k_{app} = 13.22 \times 10^{-3}$ min^{-1}), which is associated with its relatively lower band gap and favorable defect structure. The enhanced performance is linked to improved charge separation facilitated by disordered oxygen vacancies in the γ' phase.

A plausible photocatalytic mechanism is in which oxygen vacancies act as electron trapping sites, suppressing charge recombination and promoting the generation of reactive oxygen species. These findings indicate that $BiCrVO_x$ materials are promising visible light-responsive photocatalysts for the degradation of organic pollutants. Furthermore, this study provides a basis for future optimization through compositional tuning and advanced synthesis strategies to improve photocatalytic performance.

References

[1] S. Parsons, Advanced Oxidation Processes for Water and Wastewater Treatment, IWA Publishing, London, UK (2004).

[2] M.A. Rauf, M.A. Meetani and S. Hisaindee, An overview on the photocatalytic degradation of azo dyes in the presence of TiO2 doped with selective transition metals, Desalination 276 (2011) 13–27.

[3] M. Ali, I. Hussain, I. Mehmud, M. Umair, S. Hu and H.M.A. Sharif, Recent Breakthroughs and Advancements in NOx and SOx Reduction Using Nanomaterials-Based Technologies: A State-of-the-Art Review, Nanomaterials 11 (2021) 3301.

[4] B. Bai, Q. Nie, H. Wu and J. Hou, The attachment-detachment mechanism of ionic/nanoscale/microscale substances on quartz sand in water, Powder Technol. 394 (2021) 1158–1168.

[5] F. Chen, J. Ma, Y. Zhu, X. Li, H. Yu and Y. Sun, Biodegradation performance and anti-fouling mechanism of an ICME/electro-biocarriers-MBR system in livestock wastewater (antibiotic-containing) treatment, J. Hazard. Mater. 426 (2022) 128064.

[6] S.S. Yang, X.L. Yu, M.Q. Ding, L. He, G.L. Cao, L. Zhao and N.Q. Ren, Simulating a combined lysis-cryptic and biological nitrogen removal system treating domestic wastewater at low C/N ratios using artificial neural network, Water Res. 189 (2021) 116576.

[7] B. Pare, S.B. Jonnalagadda, H. Tomar, P. Singh and V.W. Bhagwat, ZnO assisted photocatalytic degradation of acridine orange in aqueous solution using visible irradiation, Desalination 232 (2008) 80–90.

[8] M. Zhang, X. Sun, C. Wang, Y. Wang, Z. Tan, J. Li and B. Xi, Photocatalytic degradation of rhodamine B using Bi4O5Br2-doped ZSM-5, Mater. Chem. Phys. 278 (2022) 125697.

[9] J.Z. Cheng, Z.R. Tan, Y.Q. Xing, Z.Q. Shen, Y.J. Zhang, L.L. Liu and S.Y. Liu, Exfoliated conjugated porous polymer nanosheets for highly efficient photocatalytic hydrogen evolution, J. Mater. Chem. A 9 (2021) 5787–5795.

[10] N.M. Mahmoodi, M. Arami and N.Y. Limaee, Photocatalytic degradation of triazinic ring-containing azo dye (Reactive Red 198) by using immobilized TiO2 photoreactor: Bench scale study, J. Hazard. Mater. 133 (2006) 113–118.

[11] A.A. Yawalkar, D.S. Bhatkhande, V.G. Pangarkar and A.A.C.M. Beenackers, Solar-assisted photochemical and photocatalytic degradation of phenol, J. Chem. Technol. Biotechnol. 76 (2001) 363–370.

[12] I.K. Konstantinou and T.A. Albanis, TiO2-assisted photocatalytic degradation of azo dyes in aqueous solution: Kinetic and mechanistic investigations: A review, Appl. Catal. B: Environ. 49 (2004) 1–14.

[13] J. You, C. Liu, X. Feng, B. Lu, L. Xia and X. Zhuang, In situ synthesis of ZnS nanoparticles onto cellulose/chitosan sponge for adsorption–photocatalytic removal of Congo red, Carbohydr. Polym. 288 (2022) 119332.

[14] A. Di Paola, E. García-López, G. Marcì and L. Palmisano, A survey of photocatalytic materials for environmental remediation, J. Hazard. Mater. 211 (2012) 3–29.

[15] N.A. Al-Areqi and S. Beg, Studies in composition and temperature dependence of phase stability in the Bi4Ag x V2–x O11–(2 x)–δ system and their influence on the oxide ion performance, Phase Transit. 85 (2012) 255–263.

[16] N.A.S, Al-Areqi, S. Beg and A. Al-Alas, Study on phase stability and oxide ion conductivity in the BIAGVOX system, J. Phys. Chem. Solids 73 (2012) 730–734.

[17] S. Beg, N.A.S. Al-Areqi, K.A. Ghaleb, A. Al-Alas and S. Hafeez, Effect of Ni (II) substitution on phase stabilization electrical properties of BICo (III) VOX. 20 oxide-ion conductor, Philos. Mag. 94 (2014) 1661–1673.

[18] V. Thakral and S. Uma, Investigation of visible light photocatalytic behavior of Bi4V2O11− δ and BIMEVOX (ME= Al, Ga) oxides, Mater. Res. Bull. 45 (2010) 1250–1254.

[19] N.A.S. Al-Areqi, A. Al-Alas, A.S. Al-Kamali, K.A. Ghaleb and K. Al-Mureish, Photodegradation of 4-SPPN dye catalyzed by Ni (II)-substituted Bi2VO5. 5 system under visible light irradiation, J. Mol. Catal. A Chem. 381 (2014) 1–8.

[20] X. Hu, P. Zhang, D. Wang, J. Jiang, X. Chen, Y. Liu and P. Li, AIEgens enabled ultrasensitive point-of-care test for multiple targets of food safety: Aflatoxin B1 and cyclopiazonic acid as an example, Biosens. Bioelectron. 182 (2021) 113188.

[21] C.X. Chen, S.S. Yang, J. Ding, G.Y. Wang, L. Zhong, S.Y. Zhao and N.Q. Ren, Non-covalent self-assembly synthesis of AQ2S@ rGO nanocomposite for the degradation of sulfadiazine under solar irradiation: The indispensable effect of chloride, Appl. Catal. B Environ. 298 (2021) 120495.

[22] X. Chen, J. Liu, H. Wang, D.Y. Ding, Y. Sun and H. Yan, One-step approach to novel $Bi_4V_2O_{11}$ hierarchical hollow microspheres with high visible-light-driven photocatalytic activities, J. Mater. Chem. 22 (2012) 877–883.

[23] G. Li, S. Huang, N. Zhu, H. Yuan, D. Ge and Y. Wei, Defect-rich heterojunction photocatalyst originated from the removal of chloride ions and its degradation mechanism of norfloxacin, Chem. Eng. J. 421 (2021) 127852.

[24] H. He, Q.Q. Zhu, Y. Yan, H.W. Zhang, Z.Y. Han, H. Sun and M. Du, Metal–organic framework supported Au nanoparticles with organosilicone coating for high-efficiency electrocatalytic N2 reduction to NH3, Appl. Catal. B Environ. 302 (2022) 120840.

[25] Y. Zheng, F. Duan, M.Q. Chen and Y. Xie, Synthetic Bi2O2CO3 nanostructures: Novel photocatalyst with controlled special surface exposed, J. Mol. Catal. A 317 (2010) 34–40.

[26] E.J. Li, K. Xia, S.F. Yin, W.L. Dai, S.L. Luo and C.T. Au, Preparation, characterization and photocatalytic activity of Bi2O3–MgO composites, Mater. Chem. Phys. 125 (2010) 236–241.

[27] H. Lin, C. Ding, K. Sato, Y. Tsutai, H. Ohtaki, M. Iguchi, C. Wada and T. Hashida, Preparation of and SDC electrolyte thin films on dense and porous substrates by modified sol-gel route, Mater. Sci. Eng. B 148 (2008) 73–76.

[28] A. Al-Alas, S. Beg, N.A.S. Al-Areqi and S. Hafeez, Influence of microwave-assisted calcination on structural properties and oxide-ion performance of layered-perovskite γ-BIMEVOX solid electrolyte synthesized by ethylene glycol-citrate sol-gel route, J. Eur. Ceram. Soc. 33 (2013) 2111–2117.

[29] S. Beg, A. Al-Alas and N.A.S. Al-Areqi, Layered Aurivillius compound: synthesis, characterization, and electrical properties, J. Alloys Compd. 504 (2010) 413–419.

[30] S. Beg, N.A.S. Al-Areqi and S. Haneef, Study of phase transition and ionic conductivity changes of Cd-substituted Bi4V2O11-δ, Solid State Ionics 179 (2008) 2260–2264.

[31] S. Beg, N.A.S. Al-Areqi, S. Hafeez and A. Al-Alas, Improved structural and electrical properties of nickel and aluminum co-doped Bi4V2O11 solid electrolyte, Ionics 21 (2015) 421–428.

[32] F. Krok, I. Abrahams, A. Zadrozna, M. Małys, W. Bogusz, J.G. Nelstrop and A.J. Bush, Electrical conductivity and structure correlation in BIZNVOX, Solid State Ionics 119 (1999) 139–144.

[33] N.A.S. Al-Areqi and S. Beg, Phase transition changes in Bi4CexV2-xO11-(x/2)-δ system, Mater. Chem. Phys. 115 (2009) 5–8.

[34] R.D. Shannon and C.T. Prewitt, Effective ionic radii in oxides and fluorides, Acta Crystallogr. B 25 (1969) 925–946.

[35] R.D. Shannon, Revised effective ionic radii and systematic studies of interatomic distances in halides and chalcogenides, Acta Crystallogr. A 32 (1976) 751–767.

[36] E. Pernot, M. Anne, M. Bacmann, P. Strobel, J. Fouletier, R.N. Vannier, G. Mairesse, F. Abraham and G. Nowogrocki, Structure conductivity of Cu and Ni-substituted Bi4V2O11 compounds, Solid State Ionics 70–71 (1994) 259–267.

[37] M. Alga, A. Ammar, R. Essalim, B. Tanouti, A. Outzourhit, F. Mauvy and R. Decourt, Study on structural, thermal, sintering and conductivity of Cu-Co doubly substituted Bi4V2O11, Ionics 11 (2005) 81–86.

[38] A. Watanabe and K. Das, Time-dependent degradation due to the gradual phase change in BICUVOX and BICOVOX oxide-Ion Conductors at temperatures below about 500°C, J. Solid State Chem. 163 (2002) 224–228.

[39] W. Wrobel, I. Abrahams, F. Krok, A. Kozanecka, M. Malys, W. Bogusz and J.R. Dygas, Electrical conductivity and phase transitions in the BICOVOX system, Solid State Ionics 175 (2004) 425–428.

[40] M. Malys, I. Abrahams, F. Krok, W. Wrobel and J.R. Dygas, Structure and conductivity in the BIZNVOX system, Solid State Ionics 179 (2008) 82–85.

[41] N.A.S. Al-Areqi, M. Umair, A.M. Senan, A. Al-Alas, A.M. Alfaatesh, S. Beg, K.-u.-R. Khan, S.A. Korma, M.T. El-Saadony, M.A. Alshehri, et al. Mesoporous Nano-Sized BiFeVOx.y Phases for Removal of Organic Dyes from Wastewaters by Visible–Light Photocatalytic Degradation. Nanomaterials 12 (2022)1383.